

Layer buckling in smectic-*A* liquid crystals and two-dimensional stripe phases

Sherwin J. Singer

Department of Chemistry, Ohio State University, Columbus, Ohio 43210-1173

(Received 13 April 1993)

Smectic-*A* liquid crystals and two-dimensional layered materials are observed to undergo a buckling instability when the system is subjected to dilative strain. In this work, we investigate the properties of the displacement fields for the buckling system that minimize a continuum free energy appropriate for the layered system. The key features observed in experiments are reproduced by the minimal-energy solutions, in particular, a transition from a sinusoidal to a chevron buckling profile and the accompanying increase in the buckling wavelength.

PACS number(s): 64.60.-i, 64.70.-p, 75.70.Kw, 83.70.Jr

Stripe phases are a common pattern of self-organization in thin magnetic films [1,2] and Langmuir monolayers [3,4]. Two-dimensional stripe phases are characterized by a periodic modulation of the order parameter in one direction. A smectic-*A* liquid crystal, viewed in a direction parallel to one of its layers, can be regarded as a two-dimensional layered system as well [5,6]. Both the magnetic films and smectic-*A* liquid crystals, when subjected to dilation in a direction perpendicular to the layers, give rise to a second modulation of the order parameter (Fig. 1) in a direction perpendicular to the original layer modulation [5,7-10]. In other words, the stripes can "buckle" when they are forced to have a layer spacing greater than their equilibrium period.

Smectic-*A* liquid crystals have been subjected to dilative strain between two parallel plates with the layers running parallel to the plates [5,10]. Stripe phases in magnetic systems are strained by changing either the temperature or the applied magnetic field in a direction which tends to decrease the equilibrium stripe spacing [7-9]. When there is no mechanism for injecting new stripe layers, the stripes buckle in order to bring the local

layer spacing closer to equilibrium.

Stripe buckling observed in magnetic systems exhibits some consistent trends [7-9]. The initial modulation appears above a certain strain threshold and is sinusoidal. As the strain increases past the threshold value the stripe modulation pattern incorporates higher Fourier modes and takes a zigzag or chevron appearance. Seul and Wolfe have made particularly revealing observations of stripe buckling in a ferrimagnetic film [8,9]. They find that the transition from sinusoidal to chevron buckling profile is accompanied by a lengthening of the buckling wavelength. The magnetic system can accomplish this wavelength increase by ejecting chevrons by a process analogous to dislocation climb. In this work we find that all these trends can be described by the standard continuum elastic free-energy density appropriate for a two-dimensional layered material. These trends are reproduced when we follow the displacement field that minimizes the continuum free energy as a function of the strain.

The complicated, long-range interactions that give rise to stripe phases in diverse materials need not be explicitly treated if one considers small, long-wavelength fluctuations about a reference stripe phase. In this case the requirement that the energy be unchanged upon undistorted rotation of the stripes places strong constraints on the form of the continuum elastic free energy [6]:

$$f = \frac{1}{\Lambda L_z} \int_{-L_z/2}^{L_z/2} dz \int_0^\Lambda dx \left\{ \frac{b}{2} \left[u_z - \frac{1}{2} u_x^2 \right]^2 + \frac{K}{2} u_{xx}^2 \right\}. \tag{1}$$

The *x* and *z* directions are parallel and perpendicular to the stripes. The system is assumed periodic in the *x* direction with period Λ . The field $u(x,z)$ describes the displacement of stripes away from their reference position in the sample. The system is taken to lie between perfectly flat walls at $z = \pm L_z/2$. The stripes lie parallel to the walls at this boundary. Hence $u(x,z)$ must be constant along the lines $z = \pm L_z/2$,

$$u_x \left(x, \pm \frac{L_z}{2} \right) = 0. \tag{2}$$

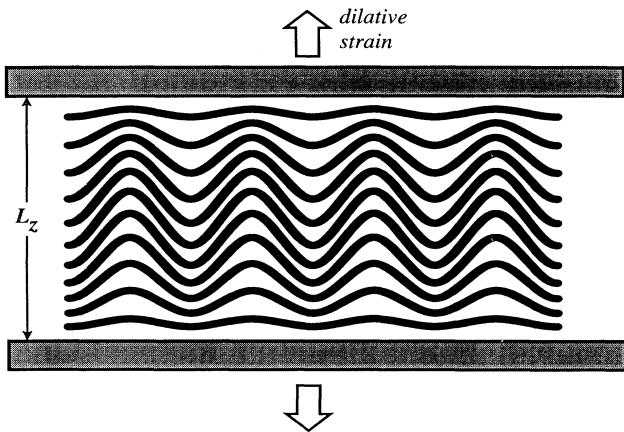


FIG. 1. Schematic representation of a layered material subjected to dilative strain.

The free energy of Eq. (1), originally developed for liquid crystals, was first applied to magnetic systems by Sornette [2]. This free-energy density is a sum of layer compression and splay contributions. The local layer spacing relative to equilibrium to all orders in \mathcal{U} is

$$[(1 + \mathcal{U}_z)(1 + \mathcal{U}_x^2)^{-1/2} - 1] = (\mathcal{U}_z - \frac{1}{2}\mathcal{U}_x^2) + \dots \quad (3)$$

Hence the free energy (1) is applicable only when \mathcal{U}_x^2 and $\mathcal{U}_z \mathcal{U}_x^2$ are small. Additional terms could be added to the free energy to enforce rotational invariance to higher orders or to describe more complicated interactions, but we would not expect these additional terms to change the qualitative aspects of the behavior we draw from the elastic free-energy density.

The purpose of this work is to explore the nature of minimal-energy configurations of the displacement field $\mathcal{U}(x, z)$ when the system is subjected to dilation in the z direction,

$$\mathcal{U}(x, z) = \alpha z + u(x, z) \quad (4)$$

The average displacement at a given z is αz , assumed linear in z , and therefore we specify

$$\int_0^\Lambda dx u(x, z) = 0 \quad (5)$$

and as a consequence of Eq. (2),

$$u \left[x, \pm \frac{L_z}{2} \right] = 0 \quad (6)$$

Remarkably, several aspects of the minimal-energy displacement fields can be understood by picturing the oscillatory motion of a classical particle in the inverted quartic potential shown in Fig. 2. The Euler equation for minimization of the continuum free energy of the layered material will be shown, in several approximate limits, to be related to Newton's equation of motion in the inverted quartic potential. As the energy of the particle rises from zero to the height of the barriers, the oscillating trajectory changes from sinusoidal to a square-wave pattern (Fig. 2). The period of oscillation steadily increases with energy and diverges logarithmically as the energy approaches the barrier height. Just to give one example, the minimal-energy buckling pattern turns out to be the time integral of these trajectories. The segments of the chevron structure with nearly constant slope are associated with stretches of the classical trajectory where the particle remains with nearly constant position near the inner turning points of the inverted quartic potential.

It is certainly an open question as to how closely experimental systems actually track minimum-free-energy configurations. We cannot discount the possibility that dynamics plays an important part in the selection of the buckling pattern. The elucidation of a relatively simple physical picture of the minimal-energy configurations for these complex systems will help separate dynamic and energetic effects. At this stage, we do not find any qualitative features of the stripe buckling experiments that are inconsistent with a description solely in terms of energetics. However, at the very least, the experimental systems may not precisely track minimum-free-energy solutions.

Also, experiments have revealed many steps in pattern evolution beyond stripe buckling [7–9, 11, 12] for which theoretical description, either dynamic or static, is far from complete. Therefore, we hardly advocate energy minimization as a universal guide for pattern selection.

We explore various approximations to minimum free energy displacement fields of the form

$$\mathcal{U}(x, z) = \alpha z + \phi(z)\psi(x) \quad (7)$$

For want of better terms, we call $\phi(z)$ the amplitude profile and $\psi(x)$ the buckling profile. Instability of the displacement field with respect to buckling into “single-mode” profiles,

$$u(x, z) \propto \cos(q_z z)\cos(q_x x) \quad (8)$$

$q_z = \pi/L_z$, $q_x = 2\pi/\Lambda$, has been analyzed previously [2, 5]. The generalization to full two-dimensional modulation of smectic layers has been given by Delrieu [13]. Since we find that the minimum-energy configuration evolves continuously from unbuckled to buckled and that the solu-

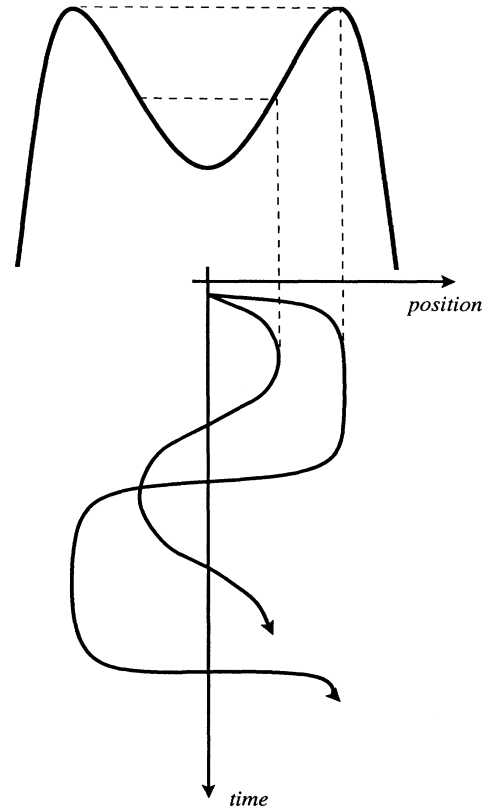


FIG. 2. An inverted quartic potential of the form that controls minimal-energy configurations of the displacement field. Two typical trajectories are shown for a classical particle oscillating in the well of this potential. The lower-amplitude trajectory is nearly harmonic. The higher-amplitude trajectory is that of a classical particle with total energy near the barrier height of the potential. The higher-energy particle spends long stretches lingering near the top of the barrier, with consequently longer periods of motion than in the harmonic case.

tions to the Euler equations have a single Fourier mode at threshold, the threshold for minimum-energy solutions turns out to be identical to the previously derived instability threshold [5].

In the following section we first relax the single-mode constraint on $\phi(z)$, keeping the buckling profile proportional to $\cos(q_x x)$. This approximation is sufficient to show how $\phi(z)$ develops from a single Fourier mode near threshold to a nearly constant function with minor edge effects as the system is pushed passed threshold. Next we explore the behavior of $u(x, z)$ in another limit, near the center of the system at $z \approx 0$. Except for very small systems, z derivatives of $u(x, z)$ should be small near the system center and equations for the buckling profile can be solved in this "bulk" limit. This second limit shows how the initial sinusoidal buckling profile evolves into a chevron or zigzag shape, increasing the modulation period during this evolution. Finally in Sec. III the two limiting cases are combined to give an approximate solution to the full displacement field.

I. MINIMAL-ENERGY AMPLITUDE PROFILE

Upon substitution of a displacement field of the form

$$\mathcal{U}(x, z) = \alpha z + \phi(z) \cos(q_x x) \quad (9)$$

into Eq. (1), a continuum free energy in terms of $\phi(z)$ and q_x is obtained:

$$f = \frac{\alpha^2 b}{2} + \frac{1}{L_z} \int_{-L_z/2}^{L_z/2} dz \left\{ \frac{1}{4} (-\alpha b q_x^2 + K q_x^4) \phi^2 + \frac{b}{4} \phi_z^2 + \frac{3b}{64} q_x^4 \phi^4 \right\}. \quad (10)$$

The boundary condition (6) forces

$$\phi \left[\pm \frac{L_z}{2} \right] = 0. \quad (11)$$

The Euler equation satisfied by the amplitude profile $\phi(z)$ which extremizes equation (10) subject to boundary conditions is

$$\phi_{zz} = \left[-\alpha q_x^2 + \frac{K}{b} q_x^4 \right] \phi + \frac{3}{8} q_x^4 \phi^3 \quad (12)$$

$$= -\frac{\partial}{\partial \phi} v(\phi), \quad (13)$$

where

$$v(\phi) = \frac{1}{2} \left[\alpha q_x^2 - \frac{K}{b} q_x^4 \right] \phi^2 - \frac{3}{32} q_x^4 \phi^4. \quad (14)$$

This is the classical equation of motion for a particle of unit mass in the inverted quartic potential $v(\phi)$. The time variable of the analogous classical motion corresponds to z in the stripe buckling problem. According to boundary conditions, we seek a trajectory that begins at $\phi=0$ at the "time" $-L_z/2$ and returns to $\phi=0$ at the later "time" $+L_z/2$. Oscillatory motion of this type will not be possible unless $v(\phi)$ exhibits a well near $\phi=0$ and hence

$$\alpha - \frac{K}{b} q_x^2 > 0. \quad (15)$$

This is the condition for solutions to the Euler equation [other than the unbuckled solution $\phi(x)=0$] to exist under *any* conditions. The conditions for solutions to exist for a specified value of system size L_z will be seen to be more restrictive.

Remarkably, the amplitude profile is not the only phenomenon related to stripe buckling that we find linked to analogous classical motion in an inverted quartic potential. It is convenient at this point to introduce a scaling of variables so that we may discuss several features in terms of a standard set of solutions to Newton's equations in a quartic potential. The required trajectories in this potential are parametrized by a single variable which we take to be ϵ , the energy divided by the peak energy of the potential. The generic equation of motion

$$m \frac{d^2 r}{dt^2} = -\frac{\partial}{\partial r} \left[\frac{1}{2} A r^2 - B r^4 \right] \quad (16)$$

is reduced by the transformations

$$r(t) = \frac{1}{2} \left[\frac{A}{B} \right]^{1/2} p(s), \quad t = 2 \left[\frac{m}{A} \right]^{1/2} s \quad (17)$$

to a standard form

$$\frac{d^2 p}{ds^2} = -\frac{\partial}{\partial p} [2p^2 - p^4]. \quad (18)$$

We chose the potential in the form $2p^2 - p^4$ because the peaks occur at $p = \pm 1$ and the magnitude of the potential at these points is unity, thereby setting a convenient energy scale in scaled coordinates so that the scaled energy variable

$$\epsilon = \frac{1}{2} \left[\frac{dp}{ds} \right]^2 + 2p^2 - p^4 \quad (19)$$

describes oscillatory motion in the range $0 \leq \epsilon < 1$. (The inconvenient feature of this choice of potential is that the coefficient of the quadratic term is not the traditional $\frac{1}{2}$.) In terms of solutions $p(s|\epsilon)$ to the scaled equations, the original equation of motion (16) for a particle with energy E has solution given by the transformation of Eq. (17) with

$$E = \frac{A^2}{16B} \epsilon. \quad (20)$$

The time of a complete period of motion in scaled coordinates is $\tau(\epsilon)$,

$$\tau(\epsilon) = 4 \int_0^{\sqrt{1-\sqrt{1-\epsilon}}} dp [2(\epsilon - 2p^2 + p^4)]^{-1/2}. \quad (21)$$

When $\epsilon \ll 1$, $\tau(\epsilon) \approx \pi$. As ϵ approaches unity $\tau(\epsilon)$ diverges logarithmically. The period of motion in terms of the parameters of the generic equation of motion (16) is $2\sqrt{m/A} \tau(\epsilon)$.

Most of the quantities needed for subsequent analysis can be expressed in terms of special functions. The derivation follows from standard classical mechanics in

one dimension and we only quote results here. The trajectory $p(s|\epsilon)$ is given implicitly as

$$s = \frac{1}{\sqrt{2\xi_+}} F \left[\theta \left| \frac{\xi_-}{\xi_+} \right. \right], \quad (22)$$

where

$$\xi_{\pm} = 1 \pm \sqrt{1-\epsilon} \quad (23)$$

and

$$\sin\theta = \frac{p}{\sqrt{\xi_-}}, \quad (24)$$

and $F(\theta|m)$ is the elliptic integral of the first kind [14]. The inner and outer turning points are $p_{\pm} = \sqrt{\xi_{\pm}}$. The boundary condition $p(0|\epsilon)=0$ is implicit in (22). The period of the motion is obtained from Eq. (22),

$$\tau(\epsilon) = 2 \left[\frac{2}{\xi_+} \right]^{1/2} K \left[\frac{\xi_-}{\xi_+} \right], \quad (25)$$

where $K(m)$ is the complete elliptic integral of the first kind [14]. Later we will use the average of several quantities over a period of the classical motion. These averages, all given in terms of the hypergeometric function $\mathcal{F}(a,b,c,x)$ [14,15], are indicated with angular brackets in the following expressions:

$$\langle p^2 \rangle_{\epsilon} = \frac{\pi \xi_-}{\tau(\epsilon) \sqrt{2\xi_+}} \mathcal{F} \left[\frac{1}{2}, \frac{3}{2}, 2, \frac{\xi_-}{\xi_+} \right], \quad (26)$$

$$\langle p^4 \rangle_{\epsilon} = \frac{3\pi \xi_-^2}{4\tau(\epsilon) \sqrt{2\xi_+}} \mathcal{F} \left[\frac{1}{2}, \frac{5}{2}, 3, \frac{\xi_-}{\xi_+} \right], \quad (27)$$

$$\langle p_s^2 \rangle_{\epsilon} = \frac{2}{\tau(\epsilon)} \int_{-p_-}^{p_-} dp \sqrt{2[\epsilon - 2p^2 + p^4]} \quad (28)$$

$$= \frac{\pi \xi_- \sqrt{2\xi_+}}{\tau(\epsilon)} \mathcal{F} \left[-\frac{1}{2}, \frac{1}{2}, 2, \frac{\xi_-}{\xi_+} \right]. \quad (29)$$

The subscript ϵ is placed on these averages as a reminder that they are functions of only one variable ϵ .

We now return to the analysis of the amplitude profile, which is the analogous trajectory generated by Eqs. (12)–(14) over a half-period of the motion. The half-period of the classical trajectory corresponds to the system dimension L_z ,

$$L_z = \frac{\tau(\epsilon_z)}{q_x} \left[\alpha - \frac{K}{b} q_x^2 \right]^{-1/2}. \quad (30)$$

The half-period in the limit of low-energy trajectories can, of course, be read from the coefficients of ϕ_{zz} and ϕ in Eq. (12) or obtained by the limit $\tau(\epsilon_z) \rightarrow \pi$ in the above expression. The half-period for the inverted quartic potential lengthens as the energy increases and diverges logarithmically as the energy nears the maxima of $v(\phi)$. Therefore the harmonic limit is a lower limit for the half-period, and it gives a lower bound on values of L_z for which solutions to the Euler equations exist,

$$L_z \geq \frac{\pi}{q_x} \left[\alpha - \frac{K}{b} q_x^2 \right]^{-1/2}. \quad (31)$$

The stripe modulation wave vector q_x that yields the shortest period of the analogous classical motion (and is able to satisfy the above inequality down to the smallest possible L_z) is

$$q_x = \left[\frac{\alpha b}{2K} \right]^{1/2} \quad (32)$$

for which the half-period is $(2\pi/\alpha)\sqrt{K/b}$. Translating Eqs. (31) and (32) into a threshold condition on α for non-trivial solutions to the Euler equation, we find the threshold dilation under these conditions to be

$$\alpha \geq \frac{2\pi}{L_z} \left[\frac{K}{b} \right]^{1/2}. \quad (33)$$

This is the same threshold found by Clark and Meyer [5] based on a stability analysis. Under the constraints imposed on the displacement field given in Eq. (9), minimal-energy solutions first appear at the point when the system first becomes unstable. At this level of approximation, buckling may be pictured as continuous in the sense of a continuous phase transition. Ribotta and Durand have experimentally confirmed the threshold criterion (33) for smectic-*A* liquid crystals [10].

The amplitude profile $\phi(z)$ of the displacement field only contains one Fourier mode in the limit of small energy E_z of the analogous classical trajectory,

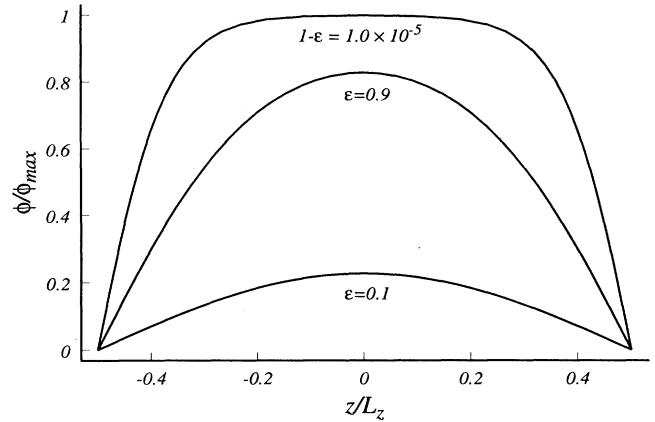


FIG. 3. Amplitude of a single buckling mode $\cos(q_x x)$ as a function of the coordinate z which runs perpendicular to the stripes or smectic layers from $z = -L_z/2$ to $L_z/2$. These amplitude profiles are parametrized by a single variable $0 \leq \epsilon < 1$. As explained in Sec. I of the text, small- ϵ solutions describe samples with small L_z , while the infinite system limit corresponds to $\epsilon \rightarrow 1$. The profiles are normalized to ϕ_{\max} [Eq. (35)], the maximum amplitude possible for a given combination of strain α , buckling wave vector q_x , and penetration length $\sqrt{K/b}$ in an infinite system.

$$E_z = \frac{2}{3} \left[\alpha - \frac{K}{b} q_x^2 \right]^2 \epsilon_z, \quad (34)$$

where we have parametrized the energy in terms of the dimensionless quantity ϵ_z according to Eq. (20). When α rises from its threshold value, a quantity which scales as $\sim L_z^{-1}$ according to Eq. (33), to typical experimental values of, say, 0.1 or 0.2, ϵ_z begins to increase. When ϵ_z is sufficiently large so that the motion samples anharmonic regions of the potential, the single-mode description of the amplitude profile no longer applies to minimal energy solutions. Several amplitude profiles for various values of ϵ_z are shown in Fig. 3. In the limit of ϵ_z near unity, which corresponds to very large z dimension L_z of a system past threshold, the analogous classical particle spends most of the time lingering near the peak of $v(\phi)$ which occurs at

$$\phi_{\max} = \left[\frac{8}{3q_x^2} \left[\alpha - \frac{K}{b} q_x^2 \right] \right]^{1/2}. \quad (35)$$

ϕ_{\max} is the amplitude of the single-mode buckling function $\cos(q_x x)$ throughout most of the sample in the limit of large L_z . Edge effects in Fig. 3 are described by the small part of the analogous classical trajectory (Fig. 2) that is spent near the bottom of the well of $v(\phi)$.

As the dilation α is driven past threshold, the modulation wave vector of the buckling profile is observed to decrease experimentally [8,9]. This is not properly described with a single-mode buckling function [$u(x, z) \propto \cos(q_x x)$]. With a single amplitude and buck-

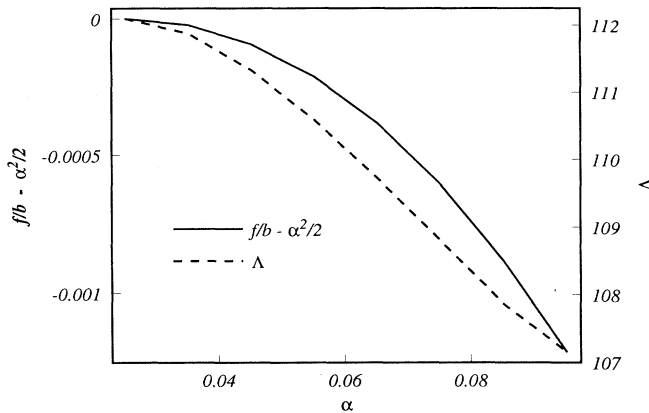


FIG. 4. The minimum free energy and energetically optimal buckling wavelength Λ , calculated for stripe buckling restricted to a single mode $\cos(q_x x)$, is plotted against the dilative strain α as the strain is increased from its threshold value, 0.025 133. Parameters chosen for this calculation are system size $L_z = 500$ and penetration length $\sqrt{K/b} = 2$. The actual units of length are irrelevant (μm would make these quantities typical of magnetic systems) since all lengths can be scaled to a particular one, for example, they can be measured in units of the penetration length $\sqrt{K/b}$. The free energy is given in the dimensionless combination f/b with the energy of the system before buckling $\alpha^2/2$ subtracted out.

ling mode, the type of continuum free energy considered in the past [2,5] the modulation wave vector q_x which minimizes the free energy *does not change* as α increases past its threshold value [16]. The picture does not improve with the amplitude profile given by the more flexible solution $\phi(z)$ to (12), but the buckling profile still proportional to $\cos(q_x x)$. Standard manipulations in the theory of action integrals in classical mechanics, used, for example, in Eq. (28), allow us to transform the free energy into the form

$$\frac{1}{b} f = \frac{\alpha^2}{2} + \frac{1}{3} \left[\alpha - \frac{K}{b} q_x^2 \right]^2 [\langle p_s^2 \rangle_{\epsilon_z} - \epsilon_z]. \quad (36)$$

When minimizing the above expression with respect to q_x , ϵ_z must be regarded a function of q_x through relation (30). When this minimization is carried out, we find that the energetically favorable q_x actually *increases* as the system is driven past threshold, as shown for a sample set of parameters in Fig. 4. This trend is *opposite* to the decrease in modulation wave vector past threshold observed experimentally [8,9]. In the next two sections, we do find agreement with the experimental trend once the single buckling mode restriction is relaxed.

II. BULK BUCKLING PROFILE

Minimal-energy displacement fields in the presence of dilative strain α satisfy the Euler equation

$$-u_{zz} + \left[\alpha - \frac{3}{2} u_x^2 \right] u_{xx} + \frac{K}{b} u_{xxxx} = 0, \quad (37)$$

where $u(x, z)$ is the excess displacement field defined in Eq. (4). In regions of the sample where u_{zz} can be neglected in comparison with the other terms, the full Euler equation reduces to a more tractable ordinary differential equation,

$$\left[\alpha - \frac{3}{2} \bar{u}_x^2 \right] \bar{u}_{xx} + \frac{K}{b} \bar{u}_{xxxx} = 0, \quad (38)$$

where $\bar{u}(x)$ is the ‘‘bulk’’ buckling profile applicable for large L_z far from system boundaries. In the single-mode case explored in Sec. I, $u_{zz} \sim L_z^{-2}$ near threshold and, except for the edges of the sample, further decreases as the strain surpasses the threshold value.

Equation (38) is simplified by the substitution

$$w(x) \equiv \bar{u}_x(x, z) \quad (39)$$

and recognizing that it indicates a conserved quantity

$$\left[\alpha - \frac{3}{2} w^2 \right] w_x + \frac{K}{b} w_{xxx} = \frac{d}{dx} \left\{ \alpha w + \frac{K}{b} w_{xx} - \frac{1}{2} w^3 \right\} = 0. \quad (40)$$

The quantity in curly brackets must be a constant,

$$\alpha w + \frac{K}{b} w_{xx} - \frac{1}{2} w^3 = \gamma = \text{const.} \quad (41)$$

Periodic boundary conditions force the constant γ to be zero, as shown below.

Equation (41) is another classical equation of motion for a particle of mass K/b in an inverted quartic potential,

$$-\gamma w + \frac{\alpha}{2} w^2 - \frac{1}{8} w^4. \quad (42)$$

We will search for periodic buckling profiles \bar{u} , and hence w must also have the same period. Because $\bar{u}(x)$ is periodic

$$\bar{u}(x + \Lambda) - \bar{u}(x) = 0 = \int_x^{x+\Lambda} dx' w(x'), \quad (43)$$

the average value of w must vanish. Since the rest of the potential is symmetric in w , this is only possible if $\gamma = 0$, leaving the final "equation of motion" for the derivative function w ,

$$\frac{K}{b} w_{xx} = -\frac{\partial}{\partial w} v(w), \quad (44)$$

where

$$v(w) = \frac{\alpha}{2} w^2 - \frac{1}{8} w^4. \quad (45)$$

In terms of solutions $p(s|\epsilon)$ to the scaled equation of motion (18), we find

$$w(x) = \sqrt{2\alpha} p \left[\frac{1}{2} \left[\frac{\alpha b}{K} x \right]^{1/2} \middle| \epsilon_x \right], \quad (46)$$

where ϵ_x is a single-parameter index to these solutions which ranges from 0 to 1. For small values of ϵ , the function $p(s|\epsilon) \approx \sqrt{\epsilon/2} \cos(2s)$. Hence the Euler equation (38) first has solutions when $q_x^2 = ab/K$. This does not contradict Eq. (32) because the approximate buckling profiles discussed in this section are essentially an infinite L_z limit. In fact, the threshold for solutions to Eq. (46) is in agreement with condition (31) in the limit of $L_z \rightarrow \infty$.

Solutions to Eqs. (44) and (45) for various values of the index ϵ_x are shown in Fig. 5. The buckling profile $\bar{u}(x)$ is nearly sinusoidal for small ϵ and tends toward a chevron or zigzag shape as ϵ_x approaches unity. The nearly-straight-line segments of the chevron shape of $\bar{u}(x)$ arise from time segments of nearly constant derivative in $w(x)$ as the analogous classical particle lingers near the peaks of the potential in Eq. (45). As the buckling profile more closely approaches a pure chevron, the slope of the profile along the nearly-straight-line segments of the chevron tends toward

$$\bar{u}_x(x) = w(x) \approx \sqrt{2\alpha}, \quad x \in (\text{chevron straight-line segment}). \quad (47)$$

This relation describes the tendency of the chevron stripes to seek the equilibrium spacing of the unstrained system. Referring back to the full order expression for the compression in Eq. (3), we see that the layers are at their equilibrium spacing (and merely rotated) when

$$u_x = \sqrt{2u_z + u_z^2}, \quad (48)$$

that is, when

$$u_x = \sqrt{2\alpha + \alpha^2}. \quad (49)$$

Equation (47) is now recognized to contain the leading-order term in the condition (49) for zero net compression along chevron stripe. The estimate (47) for u_x would be increased slightly by retaining higher-order terms in (49). Again, we are reminded that the continuum free energy (1) is only valid for small values of the derivatives.

This dimensionless quantity u_x furnishes a convenient way to estimate parameters of the quartic potential from experimental data. Seul and Wolfe recently measured the slope of chevron stripes in thin ferrimagnetic films [8,9]. They reported a value of $u_x \sim 0.71$ when $\alpha \sim 0.2$. The condition of zero net compression (49) predicts that $u_x = 0.66$ for the reported value of α , in rather good accord with experiment [8,9]. The lower-order estimate for u_x (47) that we would obtain from continuum elastic theory is 0.63. Several factors could affect this comparison with experiments. The experimental system could be slightly out of the metastable equilibrium defined by our solutions to Euler equations. Alternatively, terms higher than quartic in the free energy may have a quantitative effect. In general, the maxima of the potential $v(w)$ in Eq. (45) should match limiting slope u_x of the chevrons, and this slope should approximate Eq. (49).

The wavelength of the buckling instability Λ is given by $2\sqrt{K/\alpha b} \tau(\epsilon_x)$, where the function $\tau(\epsilon)$ is the function

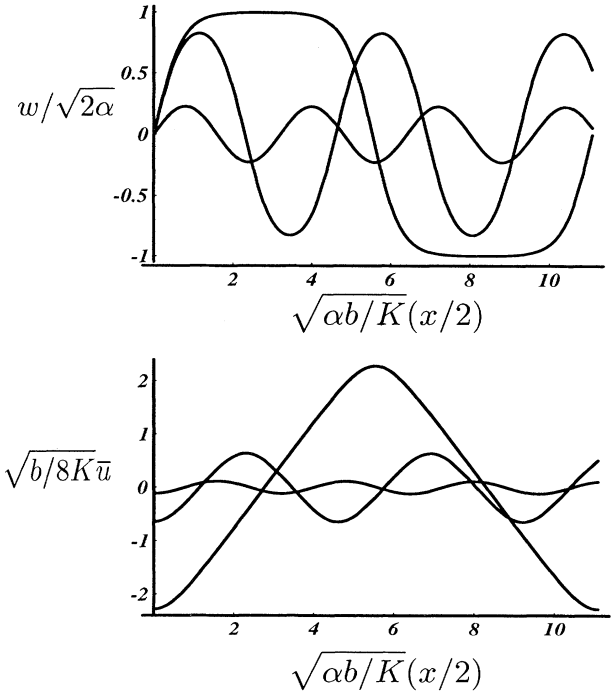


FIG. 5. Bulk buckling profile \bar{u} (lower panel) and its derivative $w(x)$ (upper panel) calculated for $\epsilon_x = 0.1, 0.9$, and $1 - 10^{-5}$. In both plots the amplitude increases with increasing ϵ_x . The functions and their arguments are scaled so that the curves only depend on ϵ_x , and the dependence on the strain α and penetration depth $\sqrt{K/b}$ is explicit.

defined in Eq. (21). It rises steeply as ϵ_x approaches unity. In agreement with recent experiments [8,9], we find that the transition from sinusoidal to chevron buckling profile is accompanied by an increase in the buckling wavelength Λ . This is a generic feature which arises when the energy of the analogous classical trajectory approaches the maxima in $v(w)$ [Eq. (45)].

The important feature to emerge from the calculations of this section is that the transition to chevron shape and increase of the modulation wavelength Λ are part of the *same* effect, which can be interpreted by physical analogy with the analogous classical particle lingering near the maxima of the inverted quartic potential $v(w)$. The tendency of Λ to increase should remain even if higher-order terms are added to the continuum free energy. One thing missing from the bulk limit explored in this section is wavelength selection. In fact, the free-energy density in the bulk is monotonically lowered as the buckling profiles $\bar{u}(x)$ evolve to the extreme chevron limit, $\epsilon_x \rightarrow 1$, even for small α . This is not surprising since the system is in effect discovering ever larger patches of unstrained, unbuckled stripe domains of size Λ in this limit. This driving force offers a physical explanation for the increase in buckling wavelength past threshold and why retaining just a single Fourier mode in the buckling profile fails to capture this effect. Wavelength selection on the basis of energetics is discussed in the following section.

III. APPROXIMATION TO THE FULL DISPLACEMENT FIELD

Our final approximation to the full displacement field is an attempt to combine the competing effects described in the first two sections, the suppression of high-order Fourier components of the buckling profile by the boundary conditions (2) and growth of the high-order modes in the form of long-wavelength chevron stripes to recapture the equilibrium layer spacing. We approximate the full displacement field by one of the form

$$\mathcal{U}(x, z) = az + \phi(z) \int^x dx' p(\frac{1}{2}q_x x' | \epsilon_x), \quad (50)$$

where $p(s|\epsilon)$ is defined in Eqs. (18) and (22)–(24). Under the ansatz of Eq. (50), the free parameters for optimization of the continuum free energy (1) are the amplitude profile $\phi(z)$, the parameter ϵ_x which controls the shape of the buckling profile (sinusoidal or chevron), and q_x , which gives additional flexibility to the buckling wavelength. The constant of integration in (50) is chosen to satisfy (5). The actual modulation wavelength of the buckled stripes is

$$\Lambda = \frac{2\tau(\epsilon_x)}{q_x}. \quad (51)$$

The usual meaning of q_x as a Fourier wave vector is only recovered in the limit of small ϵ_x : $\lim_{\epsilon_x \rightarrow 0} 2\tau(\epsilon_x)/q_x = 2\pi/q_x$.

Substituting the approximate displacement field (50) into the continuum free energy (1), we obtain

$$\begin{aligned} \frac{1}{b}f = & \frac{\alpha^2}{2} \\ & + \frac{1}{L_z} \int_{-L_z/2}^{L_z/2} dz \left\{ \frac{2}{q_x^2} \left\langle \left[\int p \right]^2 \right\rangle_{\epsilon_x} \phi_z^2 \right. \\ & \left. + \left[-\frac{\alpha}{2} \langle p^2 \rangle_{\epsilon_x} + \frac{Kq_x^2}{8b} \langle p_s^2 \rangle_{\epsilon_x} \right] \phi^2 \right. \\ & \left. + \frac{1}{8} \langle p^4 \rangle_{\epsilon_x} \phi^4 \right\}. \quad (52) \end{aligned}$$

After optimization with respect to $\phi(z)$ and again using manipulations from the theory of classical mechanical action integrals [analogous to the derivation of Eq. (36)], the free energy reduces to

$$\begin{aligned} \frac{1}{b}f = & \frac{\alpha^2}{2} + \frac{1}{2\langle p^4 \rangle_{\epsilon_x}} \left[\alpha \langle p^2 \rangle_{\epsilon_x} - \frac{Kq_x^2}{4b} \langle p_s^2 \rangle_{\epsilon_x} \right]^2 \\ & \times [\langle p_s^2 \rangle_{\epsilon_x} - \epsilon_z]. \quad (53) \end{aligned}$$

The parameter ϵ_z which controls the sharpness of the amplitude profile $\phi(z)$ is fixed by the relation between the half-period for motion of the analogous classical problem for $\phi(z)$ and the system dimension L_z ,

$$\begin{aligned} \left[\frac{1}{4 \left\langle \left[\int p \right]^2 \right\rangle_{\epsilon_x}} \left[\alpha \langle p^2 \rangle_{\epsilon_x} - \frac{Kq_x^2}{4b} \langle p_s^2 \rangle_{\epsilon_x} \right] \right]^{1/2} q_x L_z \\ = \tau(\epsilon_z). \quad (54) \end{aligned}$$

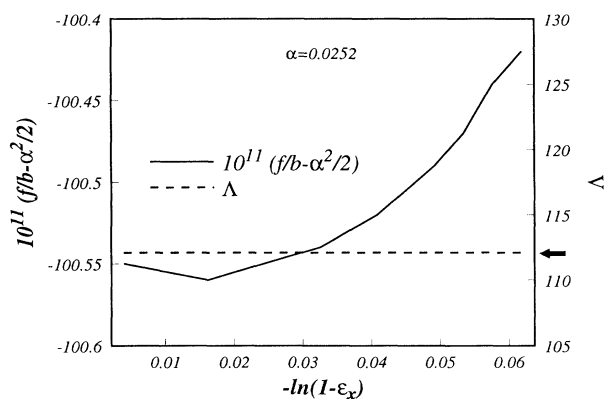


FIG. 6. The minimum value of the free-energy function in Eq. (53) with respect to q_x is shown (solid line) as a function of ϵ_x for $\alpha=0.0252$, which is just above the threshold strain $\alpha=0.025133$ for the chosen parameters $L_z=500$ and $\sqrt{K}/b=2$. (See the discussion of units of length in the caption to Fig. 4.) The plot shows that the optimal ϵ_x occurs near zero, and hence the buckling profile is sinusoidal near threshold. The dashed line is a plot of the optimal modulation wavelength [defined in Eq. (51)] as a function of ϵ_x . The buckling modulation wavelength Λ is nearly constant for ϵ_x in this range, and the global minimum occurs at $\Lambda=112.1$, indicated by an arrow on the right axis in the figure.

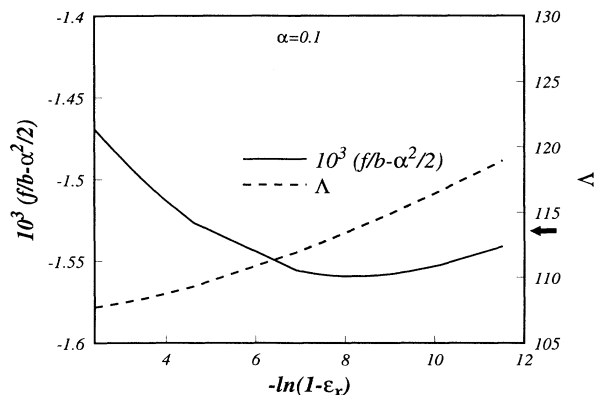


FIG. 7. The minimum value of the free-energy function in Eq. (53) with respect to q_x is shown (solid line) as a function of ϵ_x for $\alpha=0.1$ for the chosen parameters $L_z=500$ and $\sqrt{K}/b=2$. In contrast to the single-mode results shown in Fig. 4, the optimal $\epsilon_x=0.9997$, and hence the buckling profile, has more chevron than sinusoidal character. The dashed line is a plot of the optimal modulation wavelength [defined in Eq. (51)] as a function of ϵ_x . The global minimum occurs at $\Lambda=113.7$, indicated by an arrow on the right axis in the figure, slightly larger than the wavelength near threshold. Note that the less optimal single solutions ($\epsilon_x \approx 0$) have wavelength smaller than the threshold wavelength.

Since the right-hand side of this equation must be greater than or equal to π , this furnishes threshold conditions for buckling. These are easily shown in a small- ϵ_x expansion to be identical to the single-mode threshold conditions (32) and (33). In other words, we find that both ϵ_x and ϵ_z tend to zero at threshold and that only one Fourier mode is active in either the amplitude profile or buckling profile at threshold.

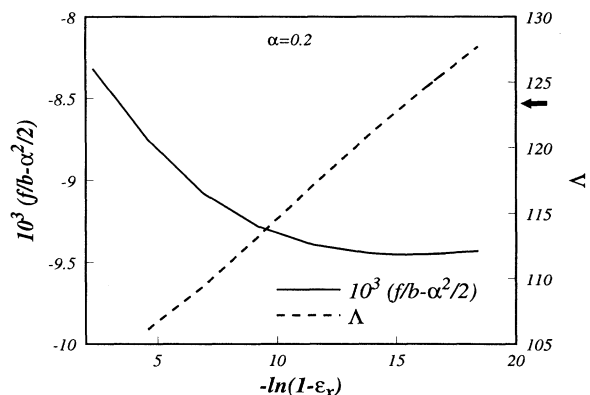


FIG. 8. The minimum value of the free-energy function in Eq. (53) with respect to q_x is shown (solid line) as a function of ϵ_x for $\alpha=0.2$ for the chosen parameters $L_z=500$ and $\sqrt{K}/b=2$. The optimal $\epsilon_x=0.999998$, and hence the buckling profile has strong chevron character. The dashed line is a plot of the optimal modulation wavelength [defined in Eq. (51)] as a function of ϵ_x . The global minimum occurs at $\Lambda=123.4$, indicated by an arrow on the right axis in the figure, roughly 10% larger than the wavelength near threshold. Note that the less optimal single solutions ($\epsilon_x \approx 0$) have wavelength smaller than the threshold wavelength.

Past threshold, Eq. (54) can be satisfied by a finite range of parameters. Numerical minimization [15] of the free energy (53) with respect to q_x leaves a function of just ϵ_x whose characteristic are shown in Figs. 6–8. The global minimum of the approximate free energy (53) is, of course, the minimum of the curves in Figs. 6–8 with respect to ϵ_x . However, it is instructive to look at the properties of the system optimized over all parameters except ϵ_x , which has the meaning of sifting through a family of buckling profiles ranging from pure sinusoidal ($\epsilon_x \rightarrow 0$) to pure chevron ($\epsilon_x \rightarrow 1$). In Figs. 6–8 we see that the optimum value of ϵ_x quickly shifts toward unity as α passes the threshold value. We also see that the buckling wavelength (51) of the optimal solutions (indicated with an arrow on the right axis in the figures) increases with α , even though the optimal wavelength of solutions with ϵ_x forced to be zero has the opposite, and incorrect, trend.

IV. DISCUSSION

Buckling undulations in dilated layered materials are controlled by two competing effects. Stripe buckling brings the layers closer together, thereby undoing the effects of the applied strain. The system can essentially recover its unstrained configuration without injecting new layers by forming zigzags or chevrons of macroscopic size. Without a boundary condition, long-wavelength, large-amplitude chevrons would be the lowest-energy response to dilative strain, even for very small strain. However, larger-amplitude chevron undulations are inconsistent with boundary conditions in which the layers lay flat at the system boundary. Layer undulation must tend toward zero at the boundaries at a sufficiently moderate rate so that large local compression is avoided. We have solved for approximate minimum energy displacement fields that describe this competition.

We have only described the initial steps in the response of a stripe phase to dilative strain. Experiments on smectic liquid crystals and magnetic materials show that past another strain threshold, the buckled stripes are unstable with respect to formation of topological defects [7–9,17–19]. Careful observation of the onset of topological defects has shown surprising regularity: Smectic liquid crystals develop an array of parabolic focal conic defects [17,18]. Magnetic films seem to support a lattice of disclination dipoles [8,9,19]. While the origin of topological defects is beyond the scope of this work, it is at least encouraging that some measure of qualitative and quantitative understanding can be brought to the early stages that lead to the proliferation of topological defects. To gain this understanding, it is essential to look beyond single-Fourier-mode descriptions of the buckling patterns.

ACKNOWLEDGMENTS

This research was partially supported by the Camille and Henry Dreyfus Foundation. We thank Michael Seul and Maggie Hurley for helpful discussions and are grateful to Michael Seul for communicating experimental results prior to publication. Anna Timosheva is thanked for helpful comments on the manuscript.

- [1] C. Kittel, *Phys. Rev.* **70**, 965 (1946); C. Kooy and U. Enz, *Phillips Res. Rep.* **15**, 7 (1960); A. A. Thiele, *J. Appl. Phys.* **41**, 1139 (1970); W. A. Barker and G. A. Gehring, *J. Phys. C* **16**, 6415 (1983); R. E. Rosensweig, M. Zahn, and R. Shumovich, *J. Magn. Magn. Mater.* **39**, 127 (1983).
- [2] D. Sornette, *J. Phys. (Paris)* **48**, 151, 1413 (1987).
- [3] H. Möhwald, *Angew. Chem.* **100**, 750 (1988).
- [4] H. M. McConnell, *Annu. Rev. Phys. Chem.* **42**, 171 (1991).
- [5] N. A. Clark and R. B. Meyer, *Appl. Phys. Lett.* **22**, 493 (1973).
- [6] P. G. de Gennes, *The Physics of Liquid Crystals* (Oxford, New York, 1975).
- [7] P. Molho, J. Gouzerh, J. C. S. Levy, and J. L. Porteseil, *J. Magn. Magn. Mater.* **54-57**, 857 (1986); P. Molho, J. L. Porteseil, Y. Souche, J. Gouzerh, and J. C. S. Levy, *J. Appl. Phys.* **61**, 4188 (1987).
- [8] M. Seul and R. Wolfe, *Phys. Rev. Lett.* **68**, 2460 (1992).
- [9] M. Seul and R. Wolfe, *Phys. Rev. A* **46**, 7519 (1992).
- [10] R. Ribotta and G. Durand, *J. Phys. (Paris)* **38**, 179 (1977).
- [11] M. Seul, L. R. Monar, L. O'Gorman, and R. Wolfe, *Science* **254**, 1616 (1991).
- [12] M. Seul, L. R. Monar, and L. O'Gorman, *Philos. Mag. B* **66**, 471 (1992).
- [13] J. M. Delrieu, *J. Chem. Phys.* **60**, 1081 (1974).
- [14] *Handbook of Mathematical Functions*, Natl. Bur. Stand. Appl. Math. Ser. No. 55, edited by M. Abramowitz and I. A. Stegun (U.S. GPO, Washington, DC, 1972).
- [15] S. Wolfram, *Mathematica* (Wolfram Research, Champaign, 1991).
- [16] S. J. Singer (unpublished).
- [17] C. S. Rosenblatt, R. Pindak, N. A. Clark, and R. B. Meyer, *J. Phys. (Paris)* **38**, 1105 (1977).
- [18] N. A. Clark and A. J. Hurd, *J. Phys. (Paris)* **43**, 1159 (1982).
- [19] M. Seul and R. Wolfe, *Phys. Rev. A* **46**, 7534 (1992).